

SPECTRAL MIXTURE ANALYSIS FOR MAPPING ABUNDANCE OF URBAN SURFACE COMPONENTS FROM THE TERRA/ASTER DATA

Ruiliang Pu, Assistant Professor
Department of Geography, University of South Florida
4202 E. Fowler Avenue, NES 107, Tampa, FL 33620
rpu@cas.usf.edu

Peng Gong, Professor and Director and **Ryo Michishita**, Graduate Student
Center for Assessment and Monitoring of Forest and Environmental Resources (CAMFER) and
Department of ESPM, University of California at Berkeley
137 Mulford Hall, University of California, Berkeley, CA 94720-3114 USA
gong@nature.berkeley.edu, r_mitch@yahoo.co.jp

ABSTRACT

Using a linear unconstrained least squares (LSS) method and a non-linear artificial neural network (ANN) algorithm, we conducted a spectral mixture analysis to the Advanced Spaceborne Thermal Emission and Reflectance Radiometer (ASTER) image data in Yokohama city, Japan, for mapping the abundance of the urban surface components. ASTER is a newly developed research facility instrument. The spectral signatures of four endmembers (Vegetation, Soil, High/Low albedo impervious surface) were extracted from the ASTER VNIR (15-m resolution) and SWIR (30-m resolution) imagery by referring to high spatial resolution airborne imagery (The Airborne Imaging Spectrometer, AISA, with 2-m resolution) and land use / land cover map for training and testing the LSS and ANN algorithms. Experimental results indicate that ASTER VNIR and SWIR image data are capable of mapping the abundances of urban surface components with a reasonable accuracy and that the ANN outperforms the unconstrained LSS in this spectral mixture analysis.

INTRODUCTION

Rapid urbanization and accelerated urban sprawl have significantly impacted on urban climate (Voogt and Oke, 2003) and on conditions of urban biophysical processes and physical environment, thus finally influencing the quality of human lives. Timely and accurate information on the status and trends of urban ecosystems and biophysical parameters is critical to developing strategies for sustainable development and to improving urban residential environment and living quality (Yang et al., 2003; Song, 2005). Therefore, developing techniques and enhancing ability for monitoring urban land use and land cover (LULC) changes are important for city modeling and planning. Ridd (1995) proposed a Vegetation-Impervious surface – Soil (V-I-S) model to parameterize urban biophysical composition and environment. In the conceptual model, the most fundamental components of the urban ecosystems can be considered by combinations of green vegetation, impervious surface materials and exposed soil within the urban area. Most unique urban surface cover types could be unmixed into some combinations of these three basic components in varying proportions.

Despite the model's limitation (e.g., it is difficult to figure out their proportion of the three basic components when they are in combination status), the vegetation, soil and impervious surface are fundamental components to construct an urban environment indeed. Vegetation abundance and distribution are primary determinants of urban environment conditions. Urban vegetation can range from highly cultivated lawns, street trees and/or horticultural plantings to remnant patches of original or regenerated native vegetation (Gong and Howarth, 1992a, b; McKinney, 2002). Urban soil component including exposed soil and/or dry vegetation (Hung and Ridd, 2002) has a distinct function from vegetation and impervious surface in an urban ecosystem, e.g., increasing aerosol concentration above urban area. Anthropogenic impervious surfaces are defined as impermeable features such as rooftops, roads, and parking lots, and these have proved to be key indicators for identifying the spatial extent and intensity of urbanization and urban sprawl (Clapham, 2003; Xian and Crane, 2005, 2006).

For monitoring the spatio-temporal dynamics of urban LULC in a timely and cost-effective manner, especially accurately and timely mapping abundance of aforementioned three components in their combination condition, data from various remote sensors are desirable. Usually, urban areas are heterogeneous and most urban image pixels at

the resolution of Landsat and similar sensors are mixed with varying proportions of different components and/or materials. In most situations, the three components in Ridd's V-I-S model (Ridd, 1995) in urban environments are mixed together within individual pixels. For example, pixels assigned as residential may represent between 20 – 100% impervious surfaces while also representing between 0 – 60% tree canopy coverage (Clapham, 2003). Therefore, conventional classification techniques are often untenable with pixels of mixed land cover composition abundant in an image (Foody, 1996) because these techniques assume that all image pixels are pure. Consequently, conventional 'hard' image classification techniques only provide a poor base for the estimation of the area extent of land-cover classes because any pixel is forced to belong to a single class. Therefore, it is desirable to decompose pixels into their components when their sizes are smaller than the pixel size. For this case, spectral mixture models and their inversion have been proposed and studied (Adams et al., 1986; Gong et al., 1994; McGwire et al., 2000; Wu and Murray, 2003; Lee and Lathrop, 2005; Lu and Weng, 2006). Among these, a linear spectral mixture model (LSM) was extensively applied to extract the abundance of various components within mixed pixels.

In previous studies, most data used for spectral mixture analysis (SMA) for monitoring and mapping urban surface components are medium-resolution Landsat TM/ETM+ images (e.g., Flanagan and Civco, 2001; Hung and Ridd, 2002; Yang et al., 2003; Wu, 2004; Song, 2005; Xian and Crane, 2005; Small and Lu, 2006) due to the fact that such data are widely accessible. With the continuing development of remote sensing technology, many new sensors come into being and data from these new sensors are available for assessment. Among them, the Advanced Spaceborne Thermal Emission and Reflectance Radiometer (ASTER) is a newly developed but widely accessible instrument with suitable spatial resolution (visible-near infrared, VNIR, 15 meters, short-wave infrared, SWIR, 30 meters, and thermal infrared, TIR, 90 meters) (Yamaguchi et al., 1998). So far, few research on SMA from ASTER data was reported, especially the SMA for mapping major urban surface materials (e.g., Lu and Weng, 2006). Therefore, in this study, we propose to assess the LSM model with an unconstrained least square solution (LSS) and artificial neural networks (ANN) for SMA to derive fractional information of vegetation, soil and impervious surface from ASTER VNIR and SWIR images acquired over Yokohama City, Japan. Because ASTER VNIR image has a relatively high spatial resolution, we also tested a 'hard' classification classifier called linear discriminant analysis (LDA) with minimum distance to identify the urban surface cover types in order to compare the unmixed results produced with the two 'soft' methods: LSS and ANN. Therefore, more specific objectives for this study include (1) evaluating the ability of ASTER data for identifying urban surface components by using SMA, and (2) comparing the performance between LSS, ANN and LDA for mapping abundance of urban surface components from the ASTER data.

STUDY AREA AND DATA SETS

Study Area

The Yokohama City, located in the central east coast of Japan, was chosen as the study area (Figure 1). With a population of over 3.5 million and a city area of 434 km², Yokohama is one of the 13 major cities designed by the Japan government ordinance. It possesses most representative urban land use / land cover (LULC) types from the central business district (CBD) to suburban to rural areas in Japan, typically found along the coast of the Pacific Ocean. During the last half of a century, the city had experienced continuous growth in population and expansion in extent and is famous for the Yokohama port, the biggest one in Japan. Right now the city is still growing. Man-made materials for buildings and roofs in the city are concrete, metal plate and brick tile. Various impervious road surfaces are covered by asphalt, concrete and rail track. Green vegetation areas are occupied by trees, shrubs, lawns in varying sizes, golf course, and crops.

Data Sets

The ASTER sensor has 14 multi-spectral bands from visible to TIR (Table 1, Yamaguchi et al., 1998). The three VNIR bands are useful for assessing vegetation and iron-oxide minerals in surface soil and rocks. The six SWIR bands were selected mainly for the purpose of surface soil and mineral mapping with 30-m pixel size. The ASTER TIR subsystem has five bands that record thermal and emissivity properties of rocks on the Earth's surface. The ASTER sensors are onboard the Terra satellite and their data, used in this study, were acquired on April 25, 2004 around 10:30 local time. Towards the objectives of this study, we would only focus on the three VNIR bands and six SWIR bands (resampled to 15-m pixel size to preserve the spatial features provided in the VNIR bands) for spectral mixture analysis (Lu and Weng, 2006). ASTER level 1B data were collected. Further image radiometric correction was undertaken by subtracting the dark object (Chavez, 1988). In this study, we subtracted digital number

(DN) = 4 (a minimum value of band 9) for every VNIR and SWIR bands because the DN of band 9 (at 2.395 μm) is assumed zero over deep pure water bodies. However, the imagery was not fully atmospherically corrected as only a single date/scene of imagery was used.

The Airborne Imaging Spectrometer (AISA) is an airborne hyperspectral system that enables imaging of 35 bands, covering the visible and NIR ranges. The AISA data, used in this analysis, were acquired on May 14, 2003 in 2-meter resolution. The AISA data set covering major part of the study area helps selecting pure pixels from ASTER VNIR image for training and testing LSM model and LDA classifier and validating spectral unmixed results. In addition, an LULC map, also covering a part of Yokohama city, was also collected for a general validation purpose.

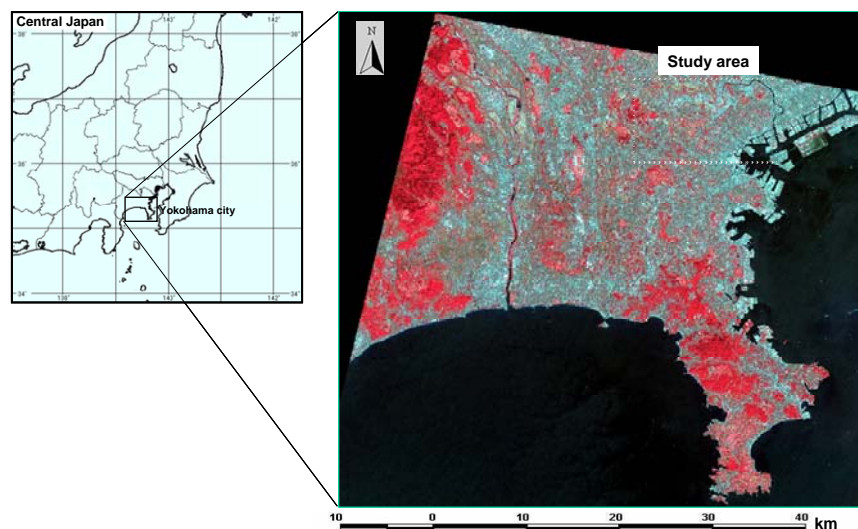


Figure 1. The location map of Yokohama city, Japan (left) and the ASTER image, acquired on April 25, 2004, shows the study area (right).

Table 1. The ASTER instrument characteristics

| Characteristics | VNIR | SWIR | TIR |
|-------------------------------|---|-------------------------------------|--------------------------------------|
| Spectral bands | Band 1: 0.52 - 0.60 μm | Band 4: 1.60 - 1.70 μm | Band 10: 8.125 - 8.475 μm |
| | Band 2: 0.63 - 0.69 μm | Band 5: 2.145 - 2.185 μm | Band 11: 8.475 - 8.825 μm |
| | Band 3N: 0.76 - 0.86 μm , Nadir looking | Band 6: 2.185 - 2.225 μm | Band 12: 8.925 - 9.275 μm |
| | Band 3B: 0.76 - 0.86 μm , Backward looking | Band 7: 2.235 - 2.285 μm | Band 13: 10.25 - 10.95 μm |
| | | Band 8: 2.295 - 2.365 μm | Band 14: 10.95 - 11.65 μm |
| Spatial resolution (m) | 15 | 30 | 90 |
| Swath width (km) | 60 | 60 | 60 |
| Radiometric resolution (bits) | 8 | 8 | 12 |

METHODOLOGY

Determination and Extraction of Endmembers

The key to successful SMA is appropriate endmember selection (Gong et al., 1994; Tompkins et al., 1997). Determination of endmembers involves identifying the number of endmembers and extracting their corresponding spectral signatures. According to feature space representation (Figure 2) of NIR – Red (B3N – B2) bands and referring to previous work (Wu and Murray, 2003; Wu, 2004; Pu et al., 2006) and Ridd's V-I-S conceptual model (Ridd, 1995), four endmembers were selected. They include Vegetation (Veg), Soil, High (Himp) and Low (Limp) albedo impervious surfaces. From Figure 2, it is apparent that spectral signatures between Himp and Soil are significantly confused, which implies that some non-linear solution to spectral mixture model might be needed.

Endmember spectra were extracted from the imagery with a common method in spectral unmixing (e.g., Adams et al., 1986; Smith et al., 1990). We first identified relatively homogeneous patches of 4-9 pixels on ASTER VNIR composite image, then referred to AISA high spatial composite image (using NIR, Red and Green bands of AISA

imagery to make a pseudo-color composite image) and LULC map to determine the pure pixel location, finally picked up one pixel DN from the 4-9 homogeneous pixels patches (usually picking up the central one). The samples (pixels) extracted from the ASTER image were divided into a training set and a test set (Table 2) with each set containing the pixel spectra and the known individual endmembers.

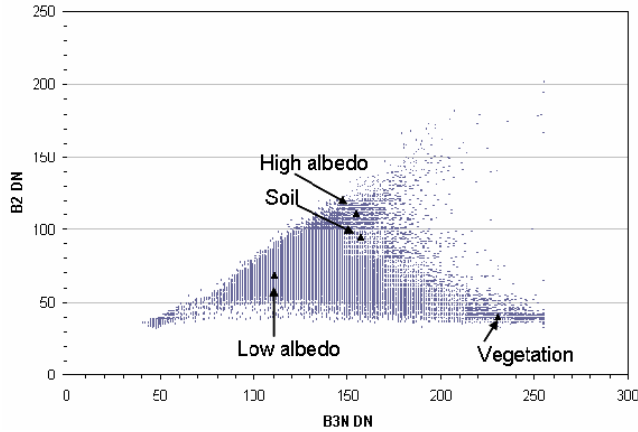


Figure 2. Feature space representation of Band 3 nadir looking – Band 2 to show the centers (dark filled triangles) of the four endmembers (Vegetation, Soil, High albedo impervious and Low albedo impervious).

Table 2. Pixel samples extracted from ASTER imagery used in this spectral mixture analysis

| Endmember | train samples | test samples | Sum |
|-----------|---------------|--------------|--------------|
| Veg | 1726 | 3451 | 5177 |
| Soil | 1053 | 2107 | 3160 |
| Himp | 1552 | 3103 | 4655 |
| Limp | 1285 | 2571 | 3856 |
| Sum | 5616 | 11232 | 16848 |

Note: Veg--vegetaion; Himp/Limp--high/low albedo impervious areas

Spectral Unmixing Methods

In the SMA, a typical linear spectral mixing model at pixel (i, j) can be expressed in equation (1):

$$\mathbf{DN}_{ij} = \mathbf{M}\mathbf{F}_{ij} + \boldsymbol{\varepsilon}_{ij} \quad (1)$$

where, a K -dimension digital-number vector, \mathbf{DN}_{ij} ; an L -dimension fraction vector \mathbf{F}_{ij} ; a $K \times L$ endmember spectra matrix \mathbf{M} ; and $\boldsymbol{\varepsilon}_{ij}$, a K -dimension error vector representing residual error. The goal of spectral unmixing is to solve for \mathbf{F}_{ij} with \mathbf{DN}_{ij} and \mathbf{M} known. When the number of endmembers in pixel (i, j) are appropriately

accounted for, \mathbf{F}_{ij} should satisfy the following conditions: $\sum_{l=1}^L \mathbf{F}_l = 1$, and $\mathbf{F}_l \geq 0$.

We used the unconstrained least squares solution (LSS) (Pu et al., 2003) to solve Eq. (1). For those fraction estimates $\hat{F}_l < 0$ and $\hat{F}_l > 1$, we simply set $\hat{F}_l = 0$ and $\hat{F}_l = 1$, respectively, and also normalized all $\hat{F}_l (l = 1, 2, \dots, L)$ to make them sum to 1 after obtaining $\hat{\mathbf{F}}_{ij}$ for every pixel in an ASTER image.

A feed-forward artificial neural network (ANN) algorithm is the second method used for unmixing mixed pixels. The network training mechanism is an error-propagation algorithm (Rumelhart et al., 1986; Pao, 1989). Similar to some of our earlier studies (Gong et al., 1996; Gong, 1996), a neural network program developed by Pao (1989) has been adapted and used in this study. In a layered structure, the input to each node is the sum of the weighted outputs of the nodes in the prior layer, except for the nodes in the input layer, which are connected to the feature values, i.e., DNs of ASTER VNIR and SWIR bands in this study. The nodes in the last layer output a vector that corresponds to similarities to each class, or fractions of endmembers within a mixed pixel. One layer between the input and output layers is usually sufficient for most learning purposes. The learning procedure is controlled by

a learning rate and a momentum coefficient that need to be specified empirically based on the results of a limited number of tests. The network training is done by repeatedly presenting training samples (pixels) with known fractions of endmembers. Network training is terminated when the network output meets a minimum error criterion or optimal test accuracy is achieved. The trained network can then be used to estimate the fraction of each endmember in a mixed pixel.

For the LSS solution, once $\hat{\mathbf{F}}_{ij}$ is obtained, the appropriateness of estimation of \mathbf{F}_{ij} can be evaluated by the root-mean-squared error *RMS* for a pixel:

$$RMS = \sqrt{\frac{1}{K} \sum_{k=1}^K \left(DN_k - \sum_{l=1}^L M_{kl} \hat{F}_l \right)^2} \quad (2)$$

The *RMS* error indicator was designed only for LSS solution.

If test samples are available (with known F_l), we can calculate the residual error *RE* for a test sample:

$$RE = \sqrt{\frac{1}{L} \sum_{l=1}^L (F_l - \hat{F}_l)^2} \quad (3)$$

where F_l is actual fraction l in a test sample. *RE* is a precision indicator for the unmixing results generated by both LSS and ANN. Due to the lack of ground truth, few studies used it (e.g., Settle and Drake, 1993).

Linear Discriminant Analysis

A linear discriminant analysis (LDA) was used as a ‘hard’ classifier for identifying each pixel as one of the four surface components (100% abundance) to compare with the unmixed results by LSS and ANN. The procedure DISCRIM in the SAS system (SAS Institute, 1991) was used.

Validation

The Yokohama LULC map, covering a part of the study area, was used to validate the spectral unmixed results of the three final endmembers (Veg, Soil and Imp (Himp + Limp)), obtained by LSS and ANN and to compare the identified result by the LDA. For those relative homogeneous patches (> 4 pixels of 15-m resolution) with similar spectral properties between ASTER VNIR image and the LULC map (complemented with AISA airborne data), a limited number of samples (point to point) were located on and extracted from fraction images and the LULC map to be compared between them. Such a process could avoid registration error at a certain degree indeed although the registration error problem could not be completely solved (Pu et al., 2003).

RESULTS AND ANALYSIS

Table 2 lists samples extracted from ASTER VNIR/SWIR images. We used the ‘holdout partition’ strategy (Manel et al., 1999; Pu and Gong, 2004) to split each endmember samples into two subsets, training set and test set. Most spectral unmixing results below were calculated from the three test sets. Figure 3 presents means (bar) and standard deviations (short line) of the first training set of the four endmembers (Veg, Soil, Himp and Limp). The means of 9 bands in the figure may construct a spectral responding matrix for spectral mixture analysis with the LSS solution.

Use of LDA

With the training samples in Table 2 and SAS DISCRIM procedure, a linear discriminant function was established. Using the discriminant function derived from the first training set, Figure 4a presents its ‘hard’ classification result of ASTER VNIR/SWIR image data. Figure 4b illustrates the distribution of the three surface components derived from the LULC map by merging neighbor LULC types similar in physical properties and referring to the normally accepted LULC classification scheme. By visual examination to both maps, the distributions of the three components are generally consistent on both maps, but it is apparent that many ‘pepper and salt’ pixels distribute across the LDA resultant map. It is very common to present such a phenomenon when a ‘hard’ classifier is executed to multispectral imagery. Since Figure 4b was derived from an LULC thematic map that was usually produced by ground survey and large-scale aerial photo interpretation, it looks cleaner. Table 3 lists

statistical results (percentage) for the three endmembers as derived with the LDA. The accuracies (in either average accuracy, AA or overall average accuracy, OAA, %) of classifying the three endmembers with the 9 ASTER bands data are relatively high (around 92% averaged from the three test samples). This is because the number of final classes has only three. However, such classification result may not be reasonable, in theory, to those spectrally mixed pixels because it does not reflect abundance of individual endmembers in the mixed pixels. More detailed comparison between the 'hard' classification result and the LULC map is presented in section 4.4 below.

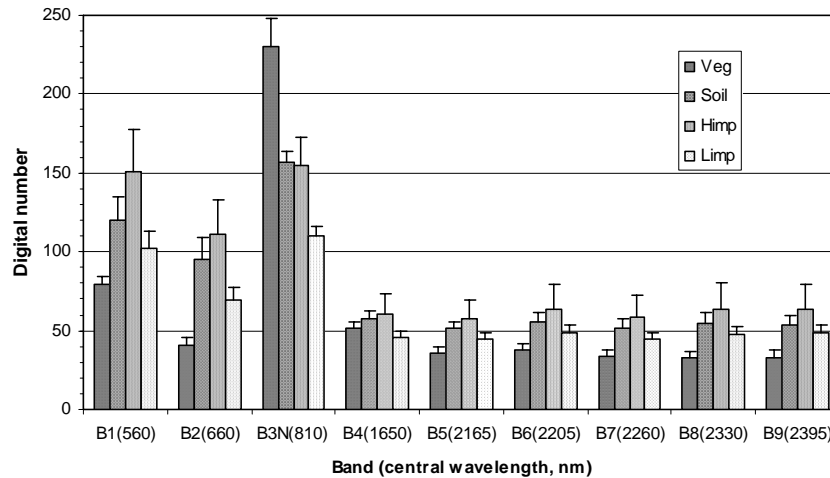


Figure 3. Means (bar) and standard deviations (short line) of the first training set of four endmembers (Vegetation, Soil, High albedo impervious and Low albedo impervious), extracted from study area. The means of 9 bands construct a spectral responding matrix for spectral mixture analysis with the unconstrained least squares (LSS) solution.

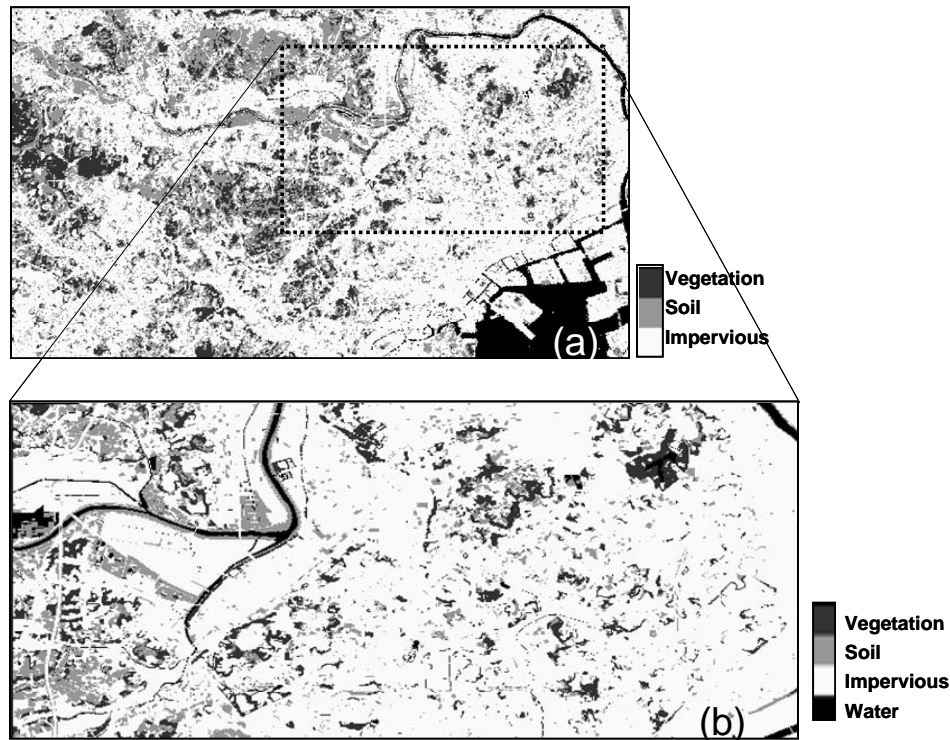


Figure 4. The 'hard' classification result with linear discriminant analysis (LDA) (a) and land use / land cover (LULC) map (b).

Table 3. Spectral unmixing (classified) results (%) produced with the three methods

| | LSS | ANN | LDA |
|-------------------|-----------|---------|-------------|
| Vegetation | 14.15 | 9.55 | 10.42 |
| Soil | 20.55 | 8.13 | 24.93 |
| Impervious | 65.30 | 82.32 | 64.65 |
| RE-train (5616) | 0.57568 | 0.05547 | n/a |
| RE-test (11232) | 0.57607 | 0.05537 | n/a |
| RME | 0.84 (DN) | n/a | n/a |
| AA/OAA (11232, %) | n/a | n/a | 91.74/91.98 |

Note: The results of RE-train and RE-test were averaged from the three sets of training and test samples, respectively. AA--average accuracy, OAA--overall average accuracy, averaged from the three sets of test samples.

Use of Unconstrained LSS

The spectral responding matrix **M** in (1) can be derived from the training sets (Table 2). Unmixing results of the ASTER VNIR/SWIR data were subsequently derived (Table 3, Figure 5). Values of column LSS in Table 3 are fractions in percentage for Vegetation, Soil and Impervious surface, respectively. From the table, the residual errors (*RE*) for both training and test samples are high (around 0.58).

Endmember images (fraction images) and the *RMS* error image generated by LSS were illustrated in Figure 5a-d. The Himp and Limp fraction images have been merged into the fraction image (Figure 5c) of the impervious surface (the same processing for ANN impervious fraction images). The range of fractions for the three endmembers has been rescaled from [0, 1] to [0, 100]. It can be seen from the Veg image for the area in the rectangle in Figure 5a that the spatial distribution of fraction of vegetation generally agrees with the Veg distribution in Figure 4b (LULC map), and the spatial distribution of the impervious area (Figure 5c) is also generally consistent with that on LULC map. However, the spatial distribution of soil fraction (Figure 5b) seems much more than that on the LULC map. This might be also related to seasonal change of urban land surface types. It looks that much impervious area has been unmixed into soil fraction due to spectral similarity between impervious and soil (Figure 2), especially much soil fraction distributing in right side of the LULC map. For the *RMS* error image (Figure 5d), the pixel values were first enlarged 10 times, then were subtracted from 255 so that the white areas in the *RMS* image indicate no error and the white to black areas in the image represent varied *RMS* error levels. It can be seen from the error image that the error is relatively low. The average *RMS* errors are shown in Table 3. An average of 0.84 DN (out of 255) for the entire study area was obtained for the LSS method. The low *RMS* error indicates that the model and the number of endmembers used are adequate. Nevertheless, the *RE* levels, calculated separately from the training and test samples, are high (Table 3). This may be caused by high confusion of Soil and Himp.

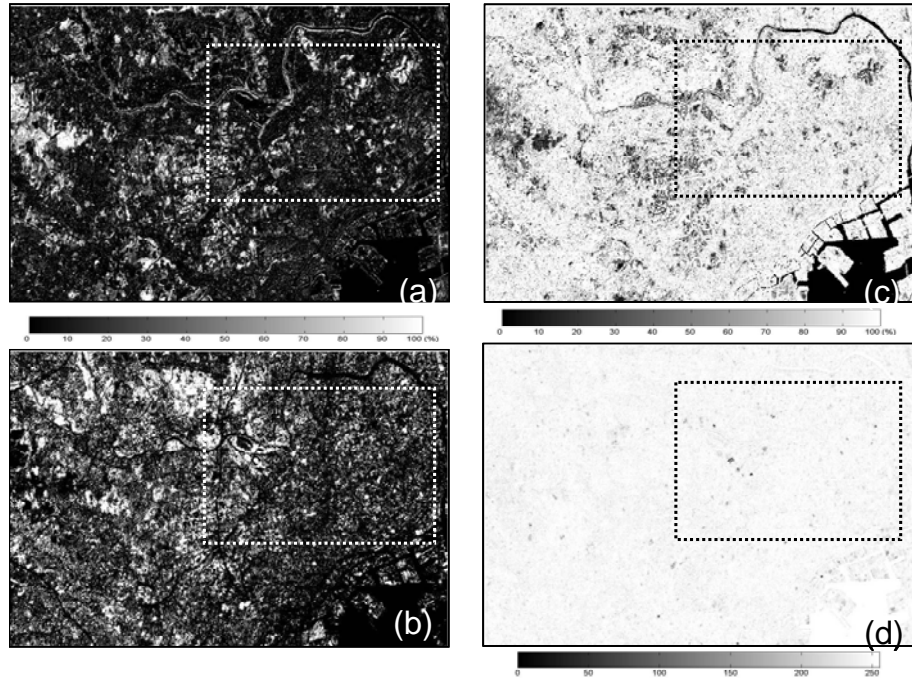


Figure 5. Spectral unmixing results with the LSS solution. (a) Vegetation fraction image; (b) Soil fraction image; (c) Impervious fraction image; and (d) *RMS* error image. The box with a white or black semitransparent line is a location of LULC map.

Use of ANN

To train and test the ANN for spectral unmixing, input DNs were first normalized to the range of [0, 1]. The nine nodes in the input layer correspond to DNs from three VNIR bands and six SWIR bands (the SWIR bands having been resampled to 15-m pixel size). The output layer had 4 nodes corresponding to 4 endmembers: Veg, Soil, Himp and Limp. They correspond to the fractions in the range of [0, 1]. To find a better ANN structure, we tested various combinations of learning rate (η), momentum coefficient (α) and number of nodes in a hidden layer. Finally, the ANN structure with a 10-node hidden layer and the learning rate $\eta = 0.5$, and momentum coefficient $\alpha = 0.7$ were used for all networks with inputs of 9 ASTER VNIR/SWIR bands.

With the same training data sets (three sets) as used to derive **M** in LSS, Figure 6 (a-c) present unmixing results using the ANN. For the purpose of display, we used the same rescaling as in Figure 5. The distribution of Veg fraction generated by ANN has a good agreement with that on the LULC map. The other two fractions (Soil and Impervious surface merged from Himp and Limp fractions) are better than those derived by LSS when compared to the LULC map. This situation is very different from Figure 5 because ANN can use subtle spectral difference between the two endmembers (Gong et al., 1997) and the ANN algorithm has a non-linear property that may be favorable to separate the two endmembers of Soil and Himp whose spectra are much overlapped (Figure 3).

The values of *RE*-train and *RE*-test with ANN, averaged from the three sets of training and test samples, respectively, compared to the LSS *RE*s, are considerably low (around 0.055 in Table 3). This indicates that the ANN is more effective than the LSS in spectral unmixing in this specific case. This conclusion is coincident with that by Pu et al. (2003).

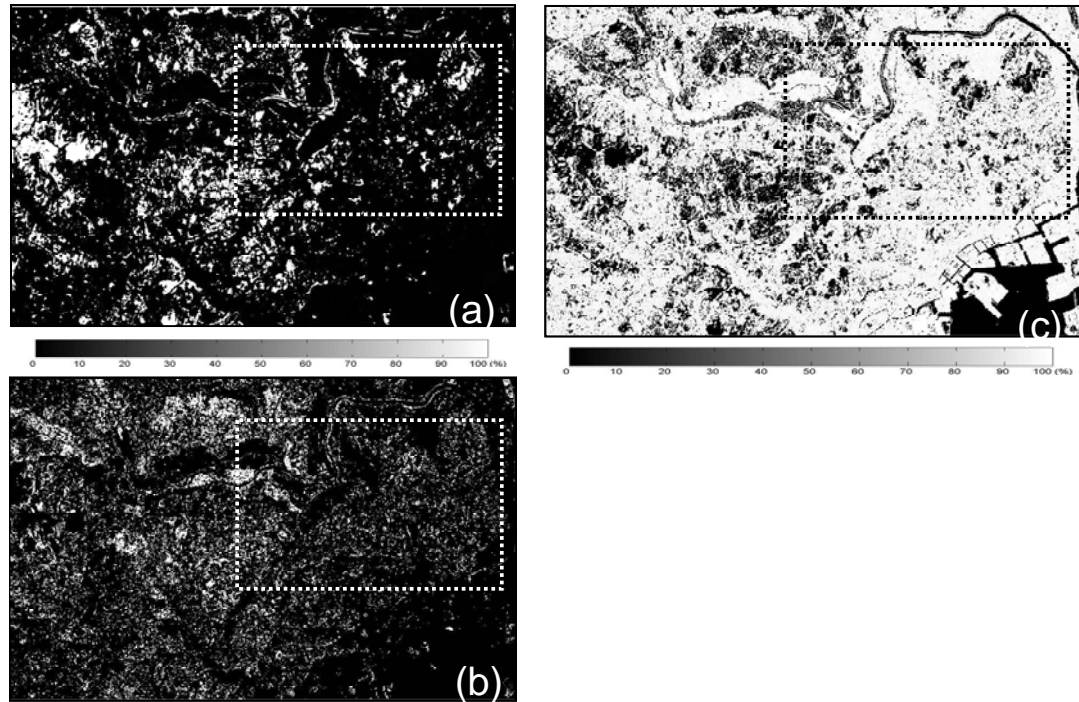


Figure 6. Spectral unmixing results using ANN. (a) Vegetation fraction image; (b) Soil fraction image; and (c) Impervious fraction image. Learning rate = 0.5, momentum coefficient = 0.7, with a 10-node hidden layer. The box with a white or black semitransparent line is a location of LULC map.

Comparison and Validation

To evaluate the performance of the two analysis methods: LSS and ANN, for spectral unmixing, on the one hand, we conducted a general comparison between unmixed results by LSS and ANN; on the other hand, we also took a close look at both sets of results. To gain an insight into the unmixed results, the ‘hard’ classification results were used as a reference. Table 4 presents general comparisons of unmixed (‘hard’) results between LSS, ANN, LDA and LULC map. In the table, the relative error for each endmember fraction was computed for each method using LULC map values as the reference (true values). The table presents that the three fractions estimated by the ANN have the lowest relative error among the three methods: LSS, ANN and LDA.

Table 4. Averaged fractions (%) of three endmembers, produced with three methods, and their relative errors (%) compared to land use/cover map

| Method | Vegetation | | Soil | | Impervious | | Sum of fraction |
|--------|------------|----------------|----------|----------------|------------|----------------|-----------------|
| | Fraction | Relative error | Fraction | Relative error | Fraction | Relative error | |
| LULC | 8.65 | 0.00 | 10.42 | 0.00 | 80.93 | 0.00 | 100.00 |
| LSS | 13.35 | 54.24 | 19.56 | 87.82 | 67.09 | -17.10 | 100.00 |
| ANN | 8.32 | -3.81 | 6.97 | -33.13 | 84.71 | 4.67 | 100.00 |
| LDA | 9.05 | 4.56 | 22.91 | 119.95 | 68.04 | -15.92 | 100.00 |

Now let us take a look at the detailed unmixing results (Figure 7). For comparison, LDA results were not used. Figure 7 illustrates a close comparison between LSS, ANN and the LULC map. The AISA imagery can serve as a detailed reference. In Figure 7, the four surface components were extracted from their typical locations. Referring to ASTER VNIR image and the AISA airborne image, obviously, the Veg image (V) from the ANN is very similar to that from LULC map, thus better than that from LSS. For Soil component (S), its distribution from ANN results is less than that from LULC map, but compared to the image (S) of AISA and ASTER VNIR, it seems more reasonable than that from LSS. For the two impervious endmember images (Hi: high albedo impervious surface and Li: low albedo impervious surface) in contrast with the corresponding AISA image, ASTER image and LULC map, apparently, the ANN results are much better than those by LSS.

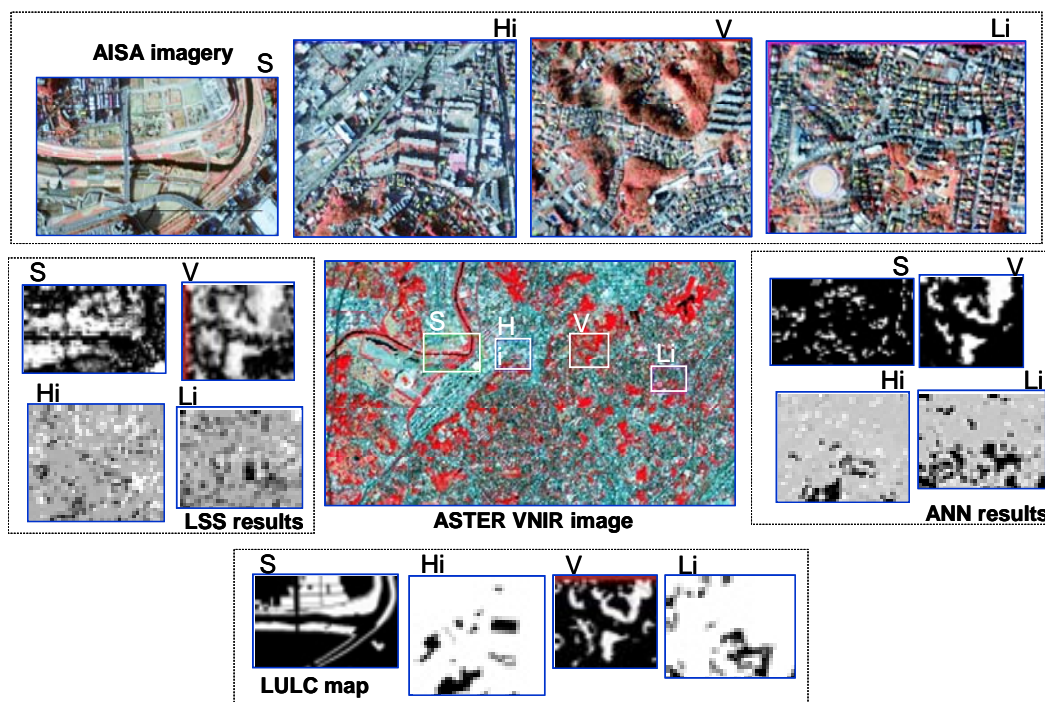


Figure 7. A close look at the spectral unmixed results and detailed comparison among the AISA airborne imagery, LULC map and ASTER spectral unmixed results. Letters V, S, Hi and Li in the figure represent the ednmember names: Veg, Soil, Himp and Limp in the text.

Figure 8 presents six scatter plots to show the agreement between fractions estimated by spectral unmixing methods and fractions interpreted from AISA image and those calculated from LULC map. The fractions from AISA interpretation and LULC map are supposed to be actual values. Due to inevitable registration errors (subpixel of ASTER VNIR), a 4-9 pixel patch where a relatively homogeneous spectral signature was required was first located over the fraction images so that a pixel picked up from the center of the patch can guarantee to be free of sub-pixel registration error. Following the procedure, a total of 85 pixel samples were extracted from both fraction images and the AISA image/LULC map. The scatter plots (Figure 8) reflect the agreement between actual value and estimated value by spectral mixture modeling. The figure shows that the agreement between actual values and estimated by ANN (see Figure 8a, 8c and 8e) is higher than that by LSS (see Figure 8b, 8d and 8f), especially for Veg fraction.

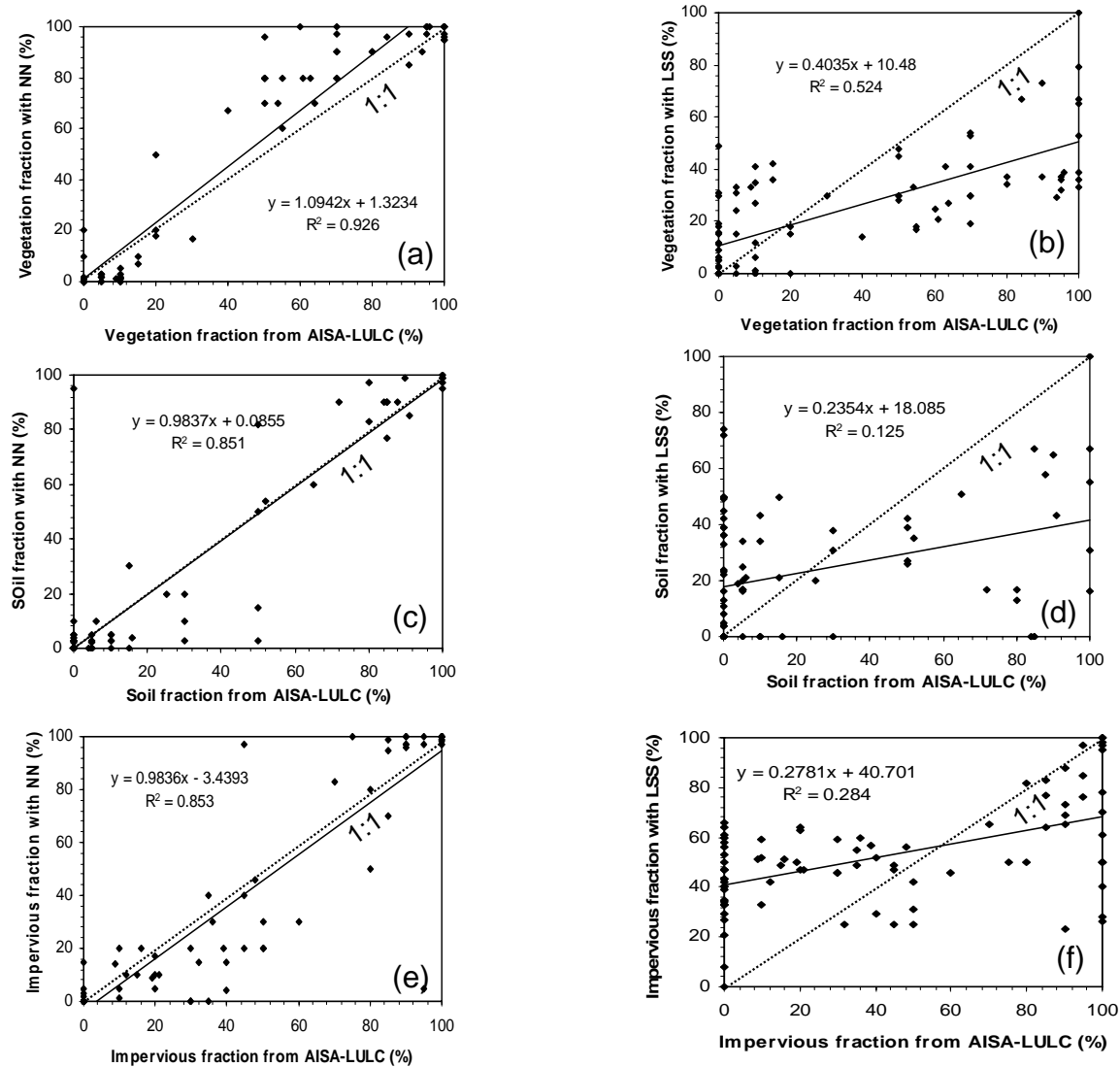


Figure 8. Validation of three endmember fractions estimated from ASTER images with those interpreted/calculated from AISA-LULC data. (a), (c) and (e) are for Vegetation, Soil and Impervious fractions estimated with the ANN, respectively, while (b), (d) and (f) are corresponding three fractions estimated with the LSS.

The preliminary validation results demonstrate that the ASTER VNIR and SWIR image data can be used to efficiently identify abundance of urban surface components, especially those generated by the ANN method. The comparison result of the two spectral mixture analysis methods: LSS and ANN, indicates that the ANN has produced higher accuracies (lower *RE* values) of endmember fractions and more reasonable spatial distribution of fractions than those by LSS. Such conclusions agree well with our previous work (Pu et al., 2003). This is because the ANN is nonlinear and it can make use of subtle spectral differences in fraction estimation for those endmembers with similar spectral properties (e.g., between Soil and Himp). This also proves that the non-linear ANN algorithm is more capable of solving the spectral mixture problem than the linear least square solution.

CONCLUSIONS

As the remote sensing technology advances, more and more data from new sensors will be available for urban environmental studies. Among them, the Advanced Spaceborne Thermal Emission and Reflectance Radiometer (ASTER) is a newly developed instrument providing images suitable for urban structure studies.

Based on our experimental results, we conclude that (1) ASTER VNIR and SWIR image data are capable of mapping the abundances of urban surface components with a reasonable accuracy and spatial agreement with the thematic map and interpretation of high resolution imagery, (2) the ANN has performed better than the unconstrained LSS when they are used to estimate abundances of the three urban surface components: Vegetation, Soil and Impervious surface at the study site, Yokohama city, Japan, from ASTER VNIR/SWIR imagery; (3) among the ANNs tested, a three-layer feed forward ANN structure with learning rate $\eta=0.5$, momentum coefficient $\alpha=0.7$ and a 10-node hidden layer performs the best. To unmix those endmembers with a certain degree of spectral signature confusion, it may be necessary to first conduct image data transformation (e.g., MNF in Wu and Murray, 2003) before conducting a spectral mixture analysis.

ACKNOWLEDGEMENTS

The research was partially supported by the grant (kzcx0504) from the Chinese Academy of Sciences, China, and the grant from the PASCO Corporation, Tokyo, Japan.

REFERENCES

- Adams, J. B., Smith, M. O., Johnson, P. E. (1986). Spectral mixture modeling: a new analysis of rock and soil types at the Viking Lander1 site. *Journal of Geophysical Research*, 91, 8098-8112.
- Chavez, P. S. (1988). An improved dark-object subtraction technique for atmospheric scattering correction of multispectral data. *Remote Sensing of Environment*, 24, 459-479.
- Clapham, Jr., W. B. (2003). Continuum-based classification of remotely sensed imagery to describe urban sprawl on a watershed scale. *Remote Sensing of Environment*, 86, 322-340.
- Flanagan, M., and Civco, D. L. (2001). Subpixel impervious surface mapping. *Proceedings of American Society for Photogrammetry and Remote Sensing Annual Convention*, St. Louis, MO, April 23-27.
- Foody, G. M. (1996). Relating the land-cover composition of mixed pixels to artificial neural network classification. *Photogrammetric Engineering & Remote Sensing*, 62, 491-499.
- Gong, P. and Howarth, P. J. (1992a). Land-use classification of SPOT HRV data using a cover-frequency method. *International Journal of Remote Sensing*, 13(8), 1459-1471.
- Gong P. and Howarth, P. J. (1992b). Frequency-based contextual classification and grey-level vector reduction for land-use identification. *Photogrammetric Engineering and Remote Sensing*, 58(4), 423-437.
- Gong, P., Miller, J. R., and Spanner, M. (1994). Forest canopy closure from classification and spectral unmixing: a multi-sensor evaluation of application to an open canopy. *IEEE Transactions on Geoscience and Remote Sensing*, 32, 1067-1080.
- Gong, P., Pu, R. and Chen, J. (1996). Mapping ecological land systems and classification uncertainty from digital elevation and forest cover data using neural networks. *Photogrammetric Engineering and Remote Sensing*, 62(11):1249-1260.
- Gong, P. (1996). Integrated analysis of spatial data from multiple sources: using evidential reasoning and an artificial neural network for geological mapping. *Photogrammetric Engineering and Remote Sensing* 62(5): 513-523.
- Gong, P., Pu, R., and Yu, B. (1997). Conifer species recognition: an exploratory analysis of *in situ* hyperspectral data. *Remote Sensing of Environment*, 62, 189-200.
- Hung, M.-C., and Ridd, M. K. (2002). A subpixel classifier for urban land-cover mapping based on a maximum-likelihood approach and expert system rules. *Photogrammetric Engineering & Remote Sensing*, 68, 1173-1180.
- Lee, S., and Lathrop, Jr., R. G. (2005). Sub-pixel estimation of urban land cover components with linear mixture model analysis and Landsat Thematic Mapper imagery, *International Journal of Remote Sensing*, 26, 4885-4905.

- Lu, D., and Weng, Q. (2006). Spectral mixture analysis of ASTER images for examining the relationship between urban thermal features and biophysical descriptors in Indianapolis, Indiana, USA. *Remote Sensing of Environment*, 104, 157-167.
- Manel, S., Dias, J.-M. and Ormerod, S. J. (1999). Comparing discriminant analysis, neural networks and logistic regression for predicting species distributions: a case study with a Himalayan river bird. *Ecological Modelling*, 120, 337-347.
- McGwire, K., Minor, T., and Fenstermaker, L. (2000). Hyperspectral mixture modeling for quantifying sparse vegetation cover in arid environments. *Remote Sensing of Environment*, 72, 360-374.
- McKinney, M. L. (2002). Urbanization, biodiversity, and conservation. *BioScience*, 52, 883-890.
- Pao, Y. (1989). *Adaptive Pattern Recognition and Neural Networks*, New York, Addison and Wesley.
- Pu, R. and Gong, P. (2004). Determination of burnt scars using logistic regression and neural network techniques from a single post-fire Landsat-7 TM imagery, *Photogrammetric Engineering & Remote Sensing*, 70, 841-850.
- Pu, R., Gong, P., Michishita, R., and Sasagawa, T. (2006). Assessment of multi-resolution and multi-sensor data for urban surface temperature retrieval. *Remote Sensing of Environment*, 104, 211-255.
- Pu, R., Xu, B., and Gong, P. (2003). Oakwood crown closure estimation by unmixing Landsat TM data. *International Journal of Remote Sensing*, 24, 4433-4445.
- Ridd, M. K. (1995). Exploring a V-I-S (vegetation-impervious surface – soil) model for urban ecosystem analysis through remote sensing: comparative anatomy for cities. *International Journal of Remote Sensing*, 16, 2165-2185.
- Rumelhart, D. E., Hinton, G. E., and Williams, R. J. (1986). Learning internal representations by error propagation. In *Parallel Distributed Processing-Explorations in the Microstructure of Cognition*, Vol. 1 (Cambridge, MA: MIT Press), pp.318-362.
- SAS Institute Inc. (1991). *SAS/STA User's Guide*, Release 6.03 Edition, Gary, NC: SAS Institute Inc., USA, 1028pp.
- Settle, J. J. and Drake, N. A. (1993). Linear mixing and the estimation of ground cover proportions. *International Journal of Remote Sensing*, 14, 1159-1177.
- Small, C., and Lu, J. W. T. (2006). Estimation and vicarious validation of urban vegetation abundance by spectral mixture analysis. *Remote Sensing of Environment*, 100, 441-456.
- Smith, M. O., Ustin, S. L., Adams, J. B., Gillespie, A. R. (1990). Vegetation in deserts: I. A regional measure of abundance from multispectral images. *Remote Sensing of Environment*, 31, 1-25.
- Song, C. (2005). Spectral mixture analysis for subpixel vegetation fractions in the urban environment: How to incorporate endmember variability? *Remote Sensing of Environment*, 95, 248-263.
- Tompkins, S., Mustard, J. F., Pieters, C. M., and Forsyth, D. W. (1997). Optimization of endmembers for spectral mixture analysis. *Remote Sensing of Environment*, 59, 472-489.
- Voogt, J. A., and Oke, T. R. (2003). Thermal remote sensing of urban climates. *Remote Sensing of Environment*, 86, 370-384.
- Wu, C. (2004). Normalized spectral mixture analysis for monitoring urban composition using ET<M+ imagery. *Remote Sensing of Environment*, 93, 480-492.
- Wu, C., and Murray, A. T. (2003). Estimating impervious surface distribution by spectral mixture analysis. *Remote Sensing of Environment*, 84, 493-505.
- Xian, G., and Crane, M. (2005). Assessment of urban growth in the Tampa Bay watershed using remote sensing data. *Remote Sensing of Environment*, 97, 203-215.
- Xian, G., and Crane, M. (2006). An analysis of urban thermal characteristics and association land cover in Tampa Bay and Las Vegas using Landsat satellite data. *Remote Sensing of Environment*, 104, 147-156.
- Yamaguchi, Y., Kahle, A. B., Tsu, H., Kawakami, T., and Pniel, M. (1998). Overview of Advanced Spaceborne Thermal Emission and Reflection Radiometer (ASTER). *IEEE Transactions on Geoscience and Remote Sensing*, 36 (4), 1062-1071.
- Yang, L., Xian, G., Klaver, J. M., Deal B. (2003). Urban land-cover change detection through sub-pixel imperviousness mapping using remotely sensed data. *Photogrammetric Engineering & Remote Sensing*, 69, 1003-1010.